

Giant Magneto-Resistive (GMR) Sensors for Non-Contacting Partial Discharge Detection

Chen, Yun; Heredia, Luis Carlos Castro; Smit, Johan J.; Niasar, Mohamad Ghaffarian; Ross, Robert

DOI

[10.1109/TIM.2023.3268485](https://doi.org/10.1109/TIM.2023.3268485)

Publication date

2023

Document Version

Final published version

Published in

IEEE Transactions on Instrumentation and Measurement

Citation (APA)

Chen, Y., Heredia, L. C. C., Smit, J. J., Niasar, M. G., & Ross, R. (2023). Giant Magneto-Resistive (GMR) Sensors for Non-Contacting Partial Discharge Detection. *IEEE Transactions on Instrumentation and Measurement*, 72, Article 6004411. <https://doi.org/10.1109/TIM.2023.3268485>

Important note

To cite this publication, please use the final published version (if applicable).
Please check the document version above.

Copyright

Other than for strictly personal use, it is not permitted to download, forward or distribute the text or part of it, without the consent of the author(s) and/or copyright holder(s), unless the work is under an open content license such as Creative Commons.

Takedown policy

Please contact us and provide details if you believe this document breaches copyrights.
We will remove access to the work immediately and investigate your claim.

Green Open Access added to TU Delft Institutional Repository

'You share, we take care!' - Taverne project

<https://www.openaccess.nl/en/you-share-we-take-care>

Otherwise as indicated in the copyright section: the publisher is the copyright holder of this work and the author uses the Dutch legislation to make this work public.

Giant Magneto-Resistive (GMR) Sensors for Non-Contacting Partial Discharge Detection

Yun Chen^{ID}, Luis Carlos Castro Heredia^{ID}, Johan J. Smit^{ID}, *Member, IEEE*,
Mohamad Ghaffarian Niasar^{ID}, and Robert Ross^{ID}, *Senior Member, IEEE*

Abstract—Partial discharge (PD) detection is a standardized technique to qualify the insulation condition in power equipment. The main purpose of the article is to evaluate the performance of an extra high-sensitivity adapted giant magneto-resistive (xMR) sensor for non-contacting PD detection. First, compensation and signal conditioning circuits of the sensor are designed. Frequency response and time-domain response to fast calibrator pulses of the sensor with the implemented circuit are measured. Besides, PD experiments based on corona and surface models are carried out and compared with measurements using a high-frequency current transformer (HFCT). The results show that the xMR system can measure the magnetic fields produced by the PDs at distances up to 50 cm. The correlation between the HFCT and xMR signals is proportional under different voltages, showing that PDs can be effectively detected and evaluated by this method. PDs in a cross-linked polyethylene (XLPE) cable with an artificial discharging defect are successfully measured, demonstrating the sensitivity and performance of the xMR system.

Index Terms—Cross-linked polyethylene (XLPE) cable, electromagnetic field measurement, giant magneto-resistive (GMR) sensor, high-frequency current transformer (HFCT), partial discharge (PD).

I. INTRODUCTION

WITH the integration of sensors into the power grid, non-contacting detection technology provides great convenience [1]. An effective diagnostic to detect the imminent failure of power equipment is provided by partial discharge

(PD) measurements [2], [3], [4]. At present, PD technology is widely used in power equipment requiring a connection into a circuit in series. However, the future development target is increasingly remote and mobile sensing technology. Therefore, it is urgent to study new non-contacting PD detection methods and develop non-intrusive sensing and intelligent failure diagnosis for power equipment.

Recently, with the rapid development of magnetic electronic devices, there have been many kinds of magnetic sensors, from Hall sensors, fluxgate sensors, and various magneto-resistive sensors to superconducting quantum interference devices (SQUID). Among these sensors, giant magneto-resistive (GMR) sensors have been widely utilized in various applications since their discovery in the 1980s, such as current sensing, non-destructive detection, magnetic data storage, position and angular sensing, and biomedical sensing [5], [6], [7], [8]. SQUID is the first choice for applications requiring the highest sensitivity. However, SQUID sensors require cooling down to cryogenic temperatures, and even with the advent of high-temperature superconductors, they involve high costs and complexity and only allow some of their components to be miniaturized. Compared to the anisotropic magneto-resistive (AMR) and Hall sensors, GMR sensors have the advantages of high sensitivity, small size, good thermal stability, and wide dynamic range [6]. Compared with the tunneling magneto-resistive (TMR) sensors, GMR sensors have relatively low noise levels to achieve a better signal-to-noise ratio [9]. GMR sensors also have become successful when integrated with state-of-the-art technologies like complementary metal-oxide-semiconductor (CMOS) and micro-electro-mechanical system (MEMS) [7]. It will overcome the technical problems of miniaturization and integration of sensing. A comparison with the sensitivities of magneto-resistive sensors from [5], [6], [10], [11], [12], [13], and [14] is shown in Fig. 1.

Several previous studies have demonstrated the versatility of GMR sensors for current measurements. In 2012, Tsinghua University designed a GMR current sensor to monitor power grids' steady-state and transient currents [13]. In 2020, Transilvania University of Brasov implemented a differential GMR system for dc/ac current measurement [15]. However, the currents studied in these articles are mainly focused on dc and low-frequency currents. The limited bandwidth of the GMR system makes it impossible to detect the PD pulse currents. In 2016, Beihang University used a GMR sensor to detect PD signals from the PD calibrator with different discharge

Manuscript received 22 October 2022; revised 12 February 2023; accepted 27 March 2023. Date of publication 19 April 2023; date of current version 4 May 2023. This work was supported in part by the European Union (EU) H2020 R&I Program and in part by the Ministry of Economic Affairs and Climate, The Netherlands, under Electronic Components and Systems for European Leadership Joint Undertaking (ECSEL JU) Grant 876659 (iRel4.0). The work of Yun Chen was supported by the China Scholarship Council (CSC) under Grant 202106150039. The Associate Editor coordinating the review process was Dr. Sasan Bakhtiari. (*Corresponding authors: Yun Chen; Johan J. Smit.*)

Yun Chen is with the High Voltage Technologies Group, Faculty of Electrical Engineering, Mathematics and Computer Science, Delft University of Technology, 2628 CD Delft, The Netherlands, on leave from the School of Electric Power Engineering, South China University of Technology, Guangzhou 510640, Republic of China (e-mail: Y.Chen-17@tudelft.nl).

Luis Carlos Castro Heredia and Mohamad Ghaffarian Niasar are with the High Voltage Technologies Group, Faculty of Electrical Engineering, Mathematics and Computer Science, Delft University of Technology, 2628 CD Delft, The Netherlands (e-mail: L.C.CastroHeredia@tudelft.nl; M.GhaffarianNiasar@tudelft.nl).

Johan J. Smit and Robert Ross are with the High Voltage Technologies Group, Faculty of Electrical Engineering, Mathematics and Computer Science, Delft University of Technology, 2628 CD Delft, The Netherlands, and also with the IWO, Institute for Science and Development, 6711 GG Ede, The Netherlands (e-mail: J.J.Smit@tudelft.nl; Rob.Ross@tudelft.nl).

Digital Object Identifier 10.1109/TIM.2023.3268485

1557-9662 © 2023 IEEE. Personal use is permitted, but republication/redistribution requires IEEE permission.
See <https://www.ieee.org/publications/rights/index.html> for more information.

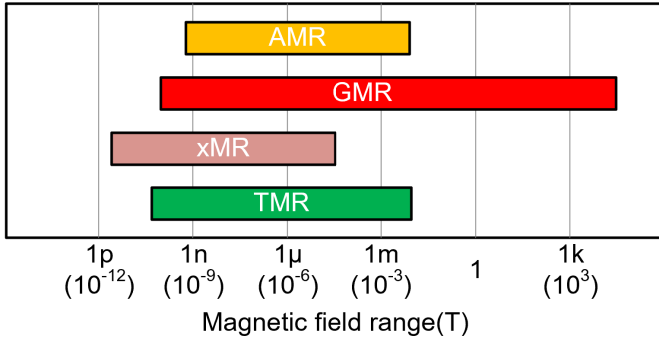


Fig. 1. Different magneto-resistive sensors and their sensitivities.

quantities and repetition rates. The minimum discharge quantity detected is 50 pC [16]. However, that paper did not focus on real PD detection. In the same year, Tsinghua University proposed using a dual-axial TMR sensor device for corona discharge location, which was easier to use than the standard probes [14]. However, that paper focuses more on PD location than identifying different PD models.

To expand the available research on this topic, our paper aims to evaluate the feasibility of a non-contacting adapted GMR sensor (TDK, model Nivio xMR sensor [17]) for PD detection and diagnosis. Compensation and signal conditioning circuits of the xMR sensor for a higher bandwidth are designed. The frequency response and time-domain response to fast calibrator pulses of the xMR system are used to verify its performance. The xMR sensor with the implemented circuits is evaluated in high-voltage (HV) experiments on PD models and a short length of cross-linked polyethylene (XLPE) cable with an artificial discharging defect.

II. GMR SYSTEM AND ITS TYPICAL PERFORMANCE

This section is divided into three subsections. First, the operation principle of the GMR sensor is presented, followed by the description of the xMR system (the xMR sensor and its associated electronic circuit), and later the experimental characterization of the typical performance of our xMR system for PD detection.

A. Operation Principle of GMR Sensor

The GMR effect is a significant change of the resistance in multilayered structures with ferromagnetic layers separated by a non-magnetic spacer due to the relative orientation of the magnetization vectors. According to different materials and structures used, GMR structures can be divided into multilayer (ML), spin valve (SV), granular alloy (GA), and magnetic tunnel junction (MTJ, also called TMR) [7].

For practical application, GMR elements are usually connected in a bridge configuration, as shown in Fig. 2 [7], including additional components like magnetic shields and flux concentrators. In typical applications, a pair of GMR resistors can be magnetically shielded and the other pair surrounded by flux concentrators. They direct the magnetic flux along the GMR unshielded resistor, which results in increased sensitivity. This configuration forms a half-bridge

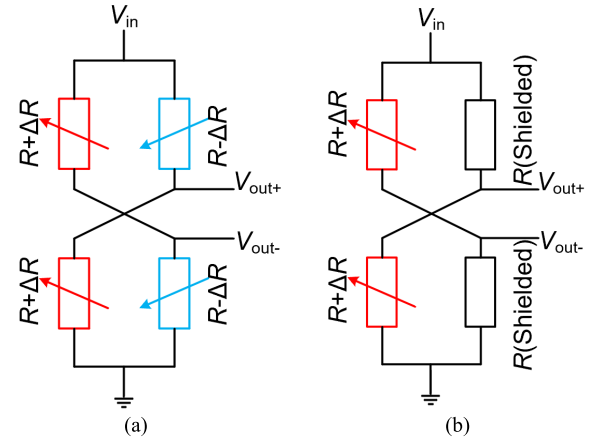


Fig. 2. Bridge structure of GMR sensors. (a) Full bridge. (b) Half bridge.

[Fig. 2(b)], and its output is scaled to the voltage supply as in the following formula.

$$V_{out+} - V_{out-} = V_{in} \cdot (\Delta R / (2R + \Delta R)) \quad (1)$$

where V_{in} is the voltage supply of the bridge, R is the base resistance when the magnetic field is null, and ΔR represents the change in resistance when an external magnetic field is applied. Typical magnetoresistance ratio (MR) levels $\Delta R/R$ of 4%–20% can be achieved in modern GMR SV structures [7]. GMR bridges built in this configuration are referred to as magnetometers due to their ability to measure magnetic field strength. This implies that the bridge output is always positive regardless of the field's orientation. However, applying field biasing techniques enables measuring ac fields with half-bridge configurations.

On the other hand, a full bridge configuration is obtained by removing the magnetic shields and the flux concentrators. As shown in Fig. 2(a), all four resistive elements are “active” but with different orientations with respect to the external magnetic field ($\pm \Delta R$). Full bridges are then known as gradiometers and are especially useful in applications where gradients of the magnetic field are to be measured. In addition, the full bridge output is bipolar and twice as large as the half-bridge configuration as in the following formula.

$$V_{out+} - V_{out-} = V_{in} \cdot (\Delta R / R). \quad (2)$$

Based on the above analysis, the full bridge is preferable due to its higher output signal and linearity. Therefore, this article chose a GMR sensor made of four GMR resistors in the full bridge, and each resistor adopts an SV element.

B. xMR System

The schematic of the xMR system is shown in Fig. 3. MR levels are typically around 10%; however, the saturation of the xMR sensor in the presence of high external magnetic fields significantly reduces its dynamic range. In order to improve its dynamic range, a compensation circuit has been implemented in our design. In Fig. 3, it can be seen a compensation coil $L1 \approx 36 \mu\text{H}$ positioned at the xMR sensor and connected in a closed-loop current configuration to

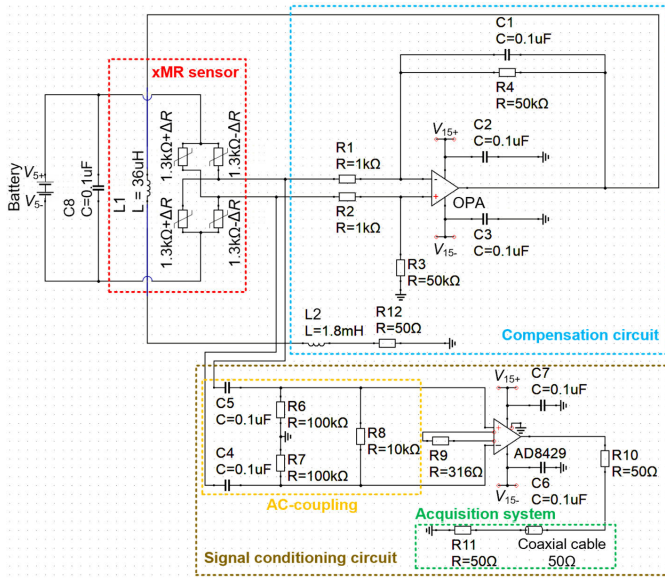


Fig. 3. Schematic of the xMR system.

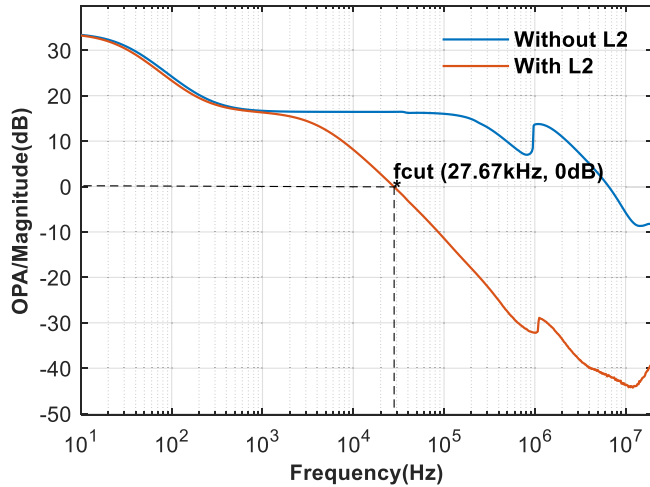


Fig. 4. Frequency response of the compensation circuit with and without L2.

compensate external magnetic fields, improve linearity, reduce hysteresis, and reduce temperature drift [18].

The compensation of the external magnetic fields is effective from dc to a cut-off frequency of $f_{\text{cut}} = 27.67$ kHz, which is obtained by a low-offset, precision operational amplifier OPA, that drives the necessary current into the compensation coil.

Although the capacitor C1 in Fig. 3 adds a pole in the frequency response of the compensation circuit, its gain is still >0 dB (~ 17 dB) up to hundreds of kHz range. For that reason, an inductor L2 = 1.8 mH is added to the compensation circuit. As a result, the 0 dB frequency is shifted down to 27.67 kHz. Above f_{cut} , the circuit gain is <0 dB rendering the compensation almost negligible, and the maximum MR level of the xMR sensor can be used to selectively react to the magnetic field created by fast pulsed signals, for instance, PD signals or transients.

A comparison of the frequency response of the compensation circuit with and without the effect of L2 can be seen in Fig. 4.

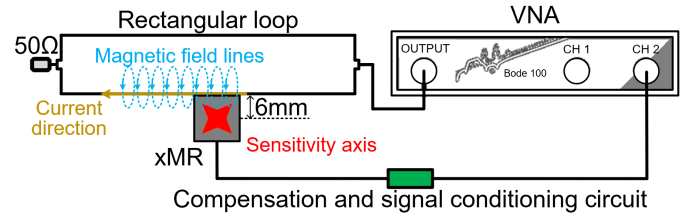


Fig. 5. Frequency response measurement set-up of the xMR system.

In turn, the xMR sensor's output is ac-coupled and amplified by the signal conditioning circuit. An instrumentation amplifier AD8429 with a high common-mode rejection ratio and a unity gain bandwidth of 15 MHz is used for this purpose.

To provide a stable power source for the xMR system and avoid switching power supply noise, the sensor and amplifiers are powered by an alkaline battery and a linear power supply, respectively.

Furthermore, to improve the transient response of the xMR, a 100 nF capacitor C8 in Fig. 3 has been added in parallel to the voltage supply of the xMR. C8 supplies the transient current drawn by the change in the xMR bridge.

C. Typical Performance

Theoretically, MR structures have bandwidths of 1 GHz due to the inherent quantum mechanism involved [19]. However, in real applications, the associated signal conditioning circuit limits the bandwidth of the whole system. The upper cut-off frequency is then set by the instrumentation amplifier AD8429, whereas the lower cut-off frequency is determined by the bandwidth of the compensation circuit.

Taking into account that the PD pulses last only for hundreds of nanoseconds, then the bandwidth of the xMR system should be wide enough to provide enough sensitivity to detect the PD pulses.

In this section, the frequency response of our xMR system is presented, as well as its time-domain response to fast calibrator pulses.

1) Frequency-Domain Response: For the characterization of our xMR system, frequency response measurements of the xMR system are conducted using a Vector Network Analyzer (VNA, Omicron Laboratory, Model Bode 100), as shown in Fig. 5. The magnetic field is generated by applying a sine wave excitation to a rectangular-shaped loop terminated with a 50 Ω resistor. The response of the xMR is measured at the output of AD8429. The source level of the VNA is 0 dBm (225 mVrms); thus, the current flowing through the loop is $225 \text{ mV}/50 \Omega = 4.5 \text{ mArms}$, and an induced magnetic field is formed in a plane perpendicular to the loop plane.

To achieve maximum sensitivity, the maximum sensitive axis of the xMR sensor must be positioned parallel to the magnetic field direction. Therefore, the xMR sensor is placed close (6 mm from the current carrying conductor) and perpendicular to the loop plane (see the red cross of the xMR sensor in Fig. 5, the sensitive axis is perpendicular to the paper). The relative position and orientation of the xMR sensor to the loop are the same when performing the time-domain response measurements.

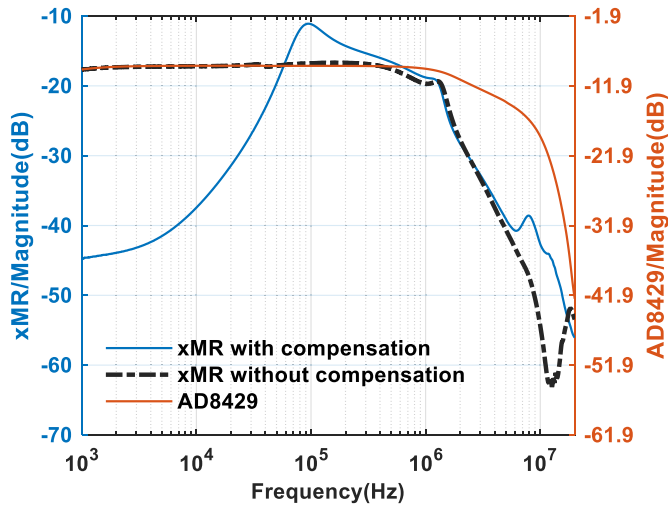


Fig. 6. Frequency response of the xMR system with and without compensation and the instrumentation amplifier AD8429.

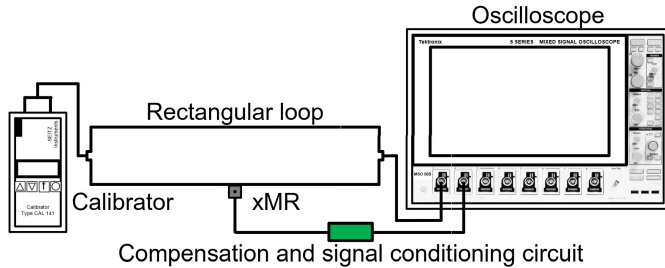


Fig. 7. Measurement set-up for the response of the xMR system to calibrator pulses.

Fig. 6 compares the frequency response of the xMR system with and without compensation. The very low-frequency signals are attenuated due to the closed-loop compensation that brings the xMR bridge output close to zero (see Fig. 4). As the frequency surpasses f_{cut} of the compensation circuit, the xMR bridge output becomes larger and amplified x20 times by the AD8429. As expected, without compensation, the xMR bridge response is flat and should be only limited by the upper cut-off frequency of AD8429.

With a gain of x20 times, the AD8429 has an upper cut-off frequency of about 10 MHz, which can also be observed in Fig. 6. Its response is measured without the xMR bridge but fed directly by a differential excitation. Although the intrinsic frequency response of the xMR bridge might be limiting the maximum bandwidth, the length of the cable connecting the xMR bridge and the associated electronic circuitry also reduces the bandwidth of the xMR system. As a consequence, the upper cut-off frequency of the xMR system is less than that of the AD8429.

2) *Time-Domain Response*: To verify the xMR system's sensitivity to PD pulses given its bandwidth and gain, a standard pulse calibrator (Seitz Instruments, Model CAL 141) is used to inject fast pulses with different amplitudes into the same rectangular-shaped loop. The outputs of both the AD8429 and the pulse calibrator are measured using an oscilloscope (Tektronix, Model MSO 58B), as shown in Fig. 7. The acquisition of the signals is made using the Fast Frame

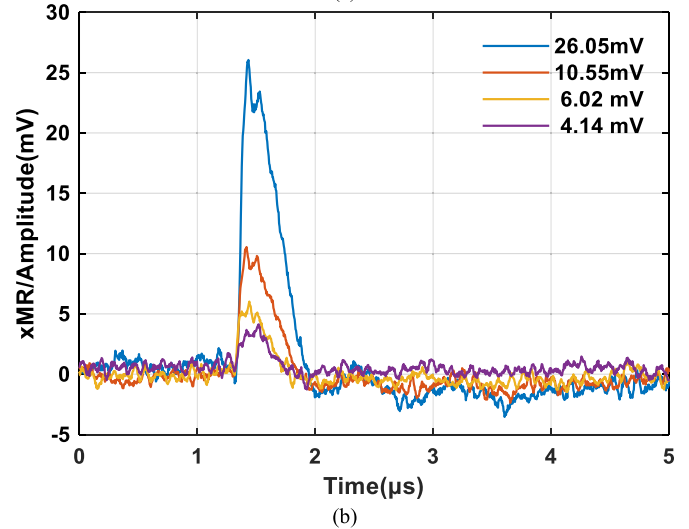
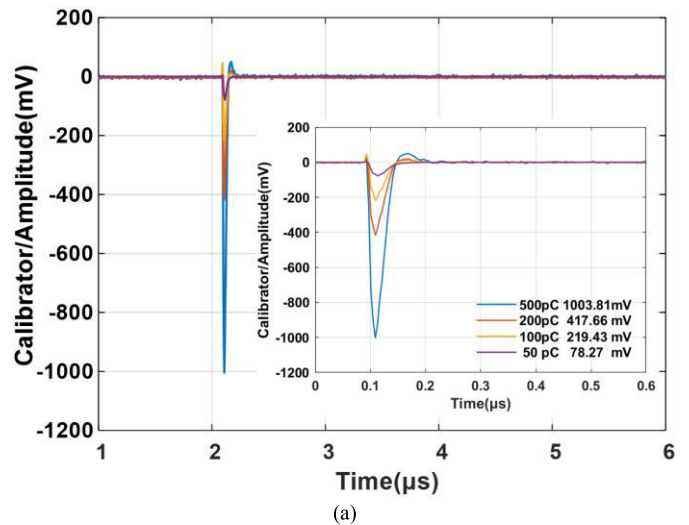


Fig. 8. xMR system's responses to calibrator pulses of different amplitudes. (a) Calibrator. (b) xMR system.

Acquisition Mode with a sampling rate of 250 MS/s and 1 M Ω input impedance. Each signal is recorded individually in a frame with a record length of 10 μ s.

The time-domain response of the xMR system versus calibrator pulses with different amplitudes is shown in Fig. 8.

As it can be seen, the xMR system output is a pulsed signal with negligible oscillations (due to the ~ 100 kHz peak in the frequency response in Fig. 6). The falling time of the calibrator signals is about 16 ns; thus, their bandwidth is no more than ~ 10 MHz. This bandwidth is still comparable to the bandwidth of the xMR system. Hence, the pulse-like waveforms in Fig. 8(b). Actual PD signals have a bandwidth extending into hundreds of MHz; therefore, as will be shown in Section IV-A, oscillations due to the 100 kHz peak will become more significant.

On the other hand, injecting signals from a calibrator allowed for a first evaluation of the sensitivity of the xMR system. Thus, with this set-up, it is possible to pick up calibrator signals of 50 pC or a current pulse of $78 \text{ mV}/50 \Omega = 1.56 \text{ mA}$ flowing along the loop. Worth mentioning that all signals are acquired with the oscilloscope

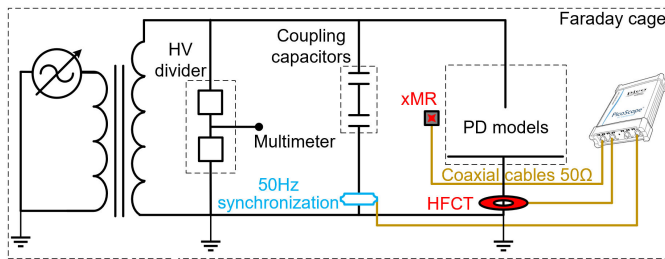


Fig. 9. Schematic of the PD experimental set-up.

in “sample mode” without any extra smoothing or filtering of the signal and in the presence of external electromagnetic interference.

III. PD EXPERIMENT

This section aims to evaluate the response (sensitivity) and performance of the xMR system to actual PD signals whose source is located at a distance from the sensor. Two types of sources will be used. The principal one is a compact PD set-up that produces corona and surface discharges (PD models). With this set-up, the discharges occur in the air without any barrier between them and the xMR sensor. The second type of source is an HV cable with an internal PD defect.

A. PD Experimental Set-Up

1) *PD Models*: The experimental set-up used to produce corona and surface discharges is shown in Fig. 9.

Two coupling capacitors of 2 nF provide a low impedance and high-frequency path for the PD signals. A high-frequency current transformer (HFCT) in series with the PD models is used to acquire the PD signals, with a bandwidth of 40 kHz–130 MHz and a gain of 9.1 mV/mA [20]. For the signal acquisition, an oscilloscope (Pico Technology, Model 6404C), with a bandwidth of 500 MHz and a sampling rate of 625 MS/s, is used.

Since, in all the experiments, the signals from the HFCT and the xMR system are recorded simultaneously, the xMR output is oversampled, adding extra high-frequency noise. However, this is unavoidable as the HFCT signals are always used as a reference or, in other words, to verify that an acquisition triggered by the xMR system corresponds to actual PDs.

The HFCT is mechanically mounted below the ground plate, while the xMR sensor is placed in different positions, as described in Fig. 10. For position 1, the sensor is placed perpendicular to the PD loop and 25 cm away from the loop's geometric center. In position 2, the xMR sensor is placed parallel to the PD loop and away from the PD models at different distances.

For the experiments, the following two PD models are used, as shown in Fig. 11:

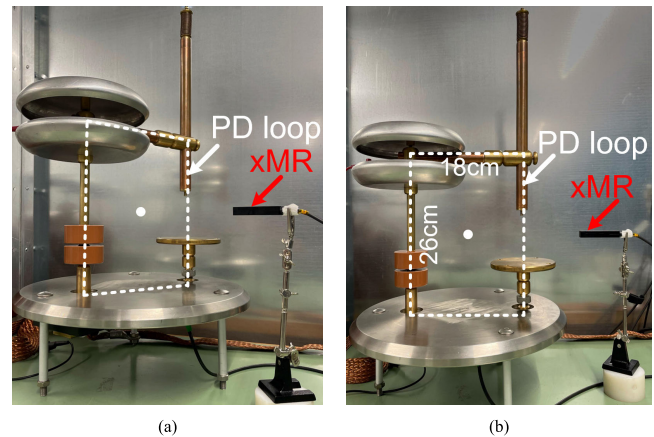


Fig. 10. Positions of the xMR sensor relative to the PD loop. (a) Position 1: the sensor is placed perpendicular to the PD loop and 25 cm away from the loop's geometric center. (b) Position 2: the xMR sensor is placed parallel to the PD loop and away from the PD models at different distances.

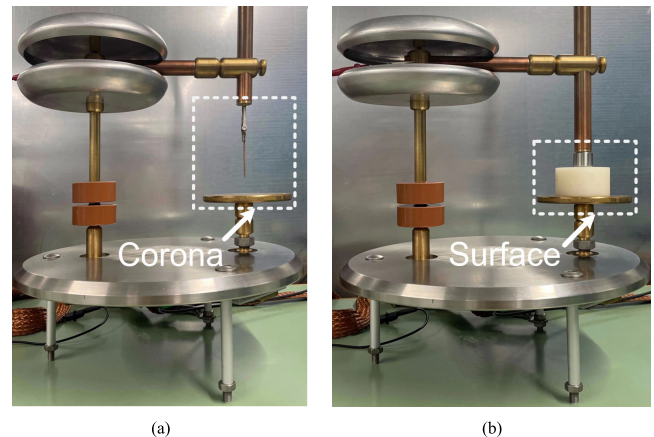


Fig. 11. PD models. (a) Corona. (b) Surface.

2) *XLPE Cable With an Artificial Defect:* As a next PD source, a defect in a 3 m long, 6/10 kV XLPE cable with outdoor cold-shrink termination and an inline splice acting as a joint is introduced for the experiments. The cable is tested and confirmed to be PD-free (<5 pC) up to $3U_0$ (18 kVrms).

A plastic tie-wrap strip is inserted at the interface between the XLPE insulation and the main insulation of the cable joint. In this way, cavities are created along the interface between XLPE insulation and the tie-wrap strip leading to internal discharges.

The experimental set-up is similar to that of the PD models in Fig. 9. A coupling capacitor of 1056 pF is connected in parallel with the cable. The xMR sensor is placed close to the grounding copper screen of the joint, as shown in Fig. 12.

B. PD Experimental Procedures

For all the experiments, the HFCT and xMR signals are recorded simultaneously. In later sections, it will be shown that in some experiments, the HFCT is used as the trigger of the oscilloscope, while in others, the xMR system is used as the trigger source. The lengths of the coaxial cables are kept similar to synchronize the peaks of each sensor output.

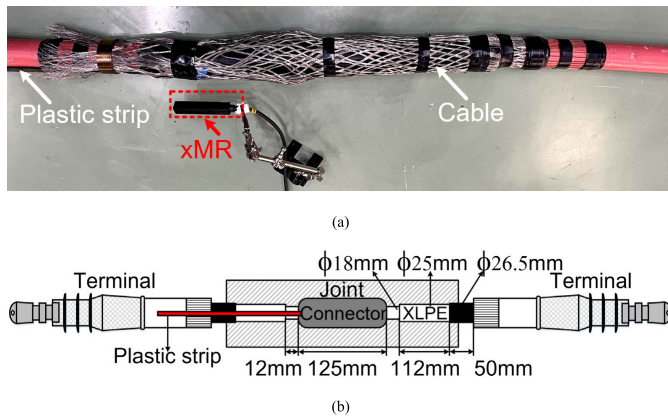


Fig. 12. XLPE cable with the artificial defect. (a) Laboratory arrangement. (b) Schematic.

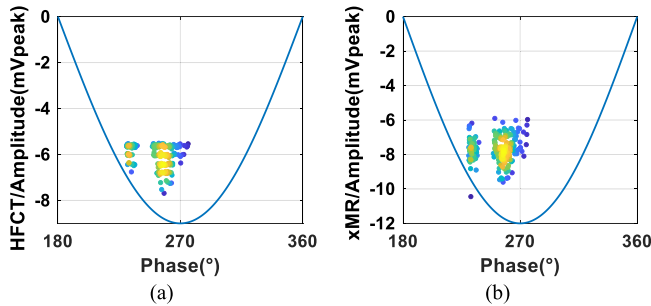


Fig. 13. PRPD patterns of the negative corona using the HFCT signals as trigger sources. (a) HFCT. (b) xMR system.

The HFCT is considered the reference signal; thus, a signal from the xMR system is regarded as a PD signal when its peak occurs almost at the same time as the peak of the HFCT signal, and its peak amplitude is roughly two times the peak of the background noise (from the starting of the recording to the time of its peak).

Two hundred waveforms for each data set are recorded and processed by the PDflex software tool [21].

IV. EXPERIMENTAL RESULTS AND DISCUSSIONS

In this section, the phase-resolved PD (PRPD) patterns and PD pulses of the PD models and the HV cable, are reported to verify the sensitivity and performance of the xMR system.

A. PD Models

Corona has some typical features. The signals have a stable amplitude, and the PD inception voltage (PDIV) is generally low for negative corona. During the experiments, negative corona pulses are produced at a voltage of 5.24 kVrms. First, the PRPD patterns obtained from the HFCT and the xMR system are depicted in Fig. 13 using the HFCT signals as the trigger sources.

In addition, the maximum and minimum waveforms from the HFCT and the xMR system, corresponding to the same trigger event, are compared, as shown in Fig. 14. The maximum and minimum amplitude from the xMR system is 7.87 and 5.12 mV, respectively.

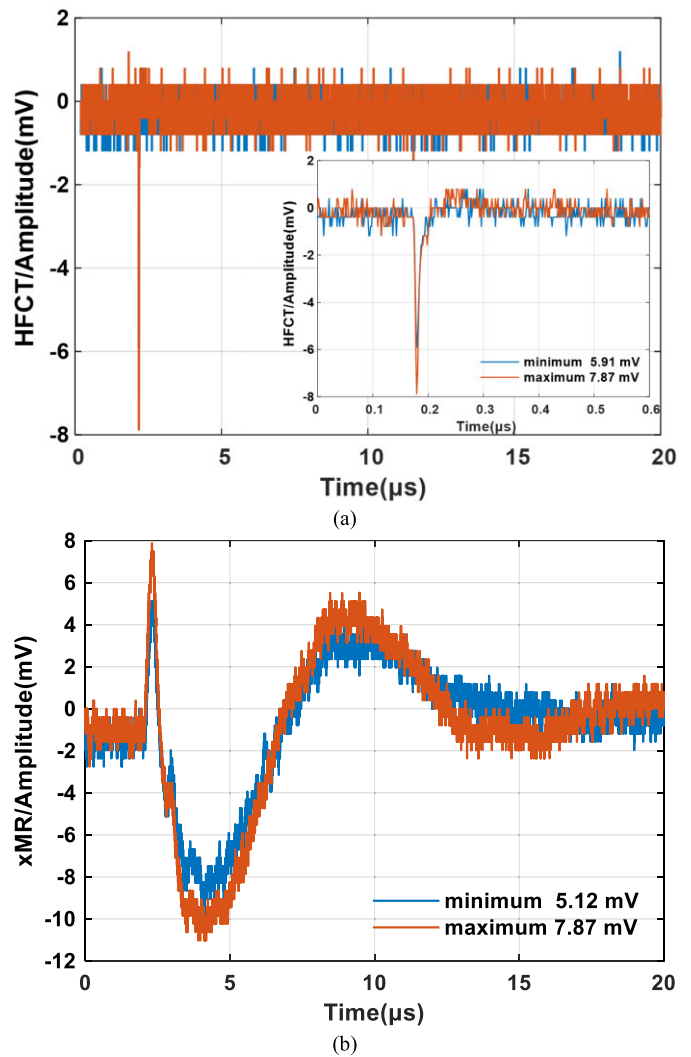


Fig. 14. Maximum and minimum corona PD pulses. (a) HFCT. (b) xMR system.

Note that the polarity of the pulses from the xMR system is reversed compared to that of the HFCT because of the relative orientation of the xMR sensor with respect to the corona. However, in Fig. 13, the PRPD patterns obtained from the HFCT and the xMR system have the same polarity because the xMR signals have been multiplied by -1 so that the PRPD pattern of the xMR system can be more visually compared with the PRPD pattern of the HFCT. The PRPD patterns of the xMR system from other experiments described in this section and Section IV-D are all processed the same way.

Next, the PRPD patterns when using the xMR signals as the trigger sources are shown in Fig. 15. A signal from the xMR system is considered a true PD signal acquisition only if the corresponding signal from the HFCT has a reference waveform like the one in Fig. 14(a). Compared to the PRPD patterns in Fig. 13, the HFCT's PRPD patterns have almost the same amplitude of 6–8 mV, which verifies that the acquisition is correct and the xMR system is properly acquiring PD signals.

After that, PD experiments are repeated with the surface PD source. During the experiments, surface discharges are produced at 8.71 kVrms. The PRPD patterns obtained from

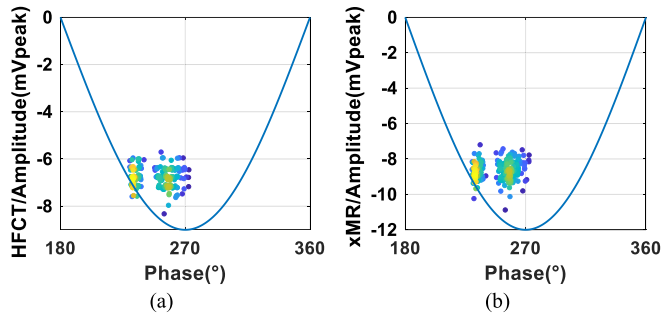


Fig. 15. PRPD patterns of the negative corona using the xMR signals as trigger sources. (a) HFCT. (b) xMR system.

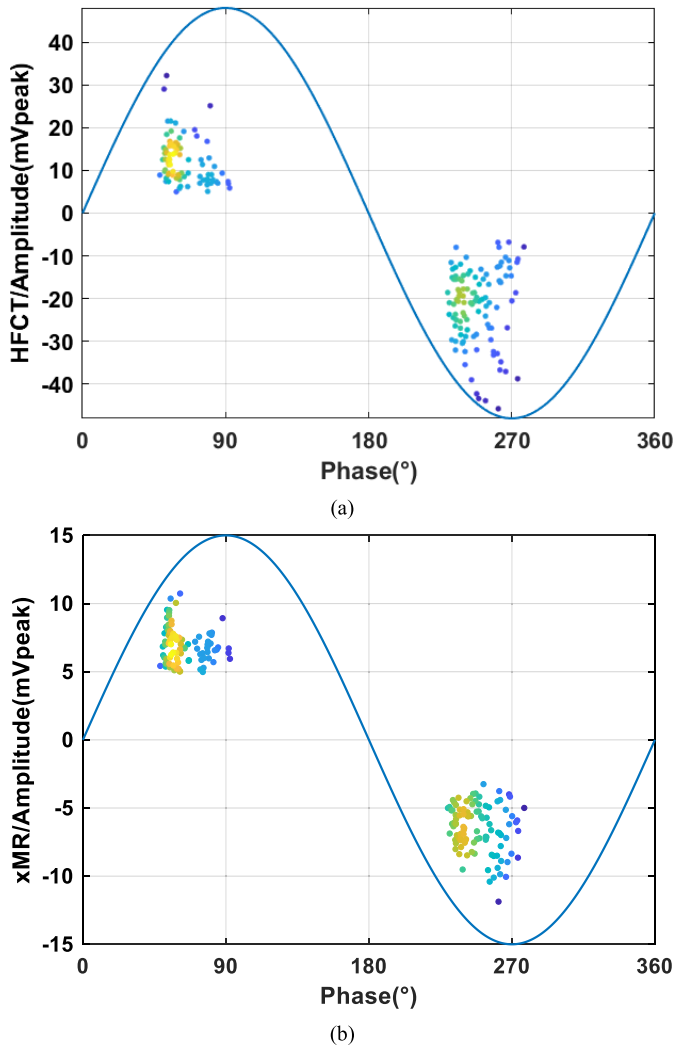


Fig. 16. PRPD patterns of the surface using the xMR signals as trigger sources. (a) HFCT. (b) xMR system.

the HFCT and the xMR system are depicted in Fig. 16, again using the xMR signals as the trigger sources.

The results confirm that the xMR system can properly detect the PD signals created by the surface. Note that the output of the xMR system is bipolar and reacts correspondingly to the polarity of the PD signals.

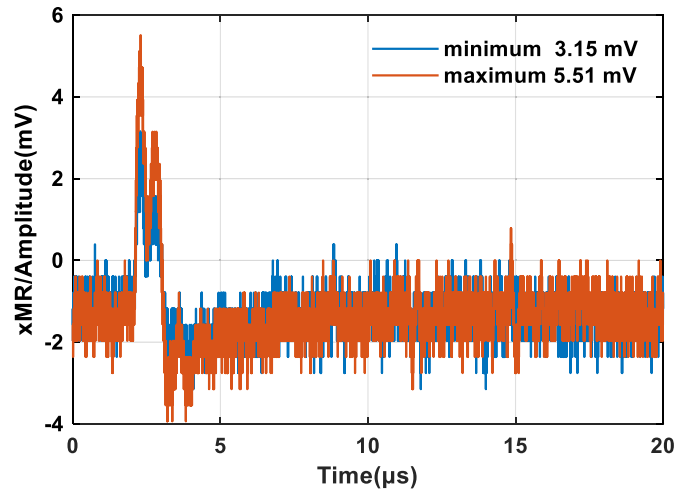


Fig. 17. Maximum PD pulses from the xMR system without compensation.

Thus, the first validation of the proper functioning of the xMR system comes from the good matching of the PRPD pattern obtained from the xMR system and the one obtained from the HFCT.

B. Comparison of the xMR System With and Without Compensation

The waveforms in Fig. 14 are characterized by a ~ 100 kHz oscillation that corresponds to the frequency peak appearing in the frequency response of the xMR system in Fig. 6. This peak is the result of the compensation circuit that produces a high-pass filter characteristic in the xMR system response. To prove it, the compensation circuit is disconnected, and the corona PD experiments are repeated.

When the xMR system works without compensation, the waveform is shown in Fig. 17, with an amplitude of 5.51 mV. Compared to the xMR system's waveform with compensation in Fig. 14(b), the waveform is now more pulse-like in accordance with the flat frequency response without compensation shown in Fig. 6.

In particular, if the xMR system is utilized in field tests with large amounts of dc or low-frequency magnetic fields, then the xMR system goes into saturation easily. This also holds true for laboratory environments. For this particular experiment, the test set-up is orientated away from external magnetic fields to avoid the saturation of the sensor.

C. Correlation Between xMR and Actual PD Signals

In this section, extra experiments at different voltages and distances are conducted to extend the PD amplitude of the data sets and experimentally evaluate the extent to which the amplitude of the xMR system follows the amplitude of the HFCT output.

The correlation between the amplitude of the HFCT and xMR signals of corona and surface discharges under different voltages is shown in Fig. 18.

The first significant result is that the polarity of the xMR signals is 100% matching the polarity of the HFCT signals.

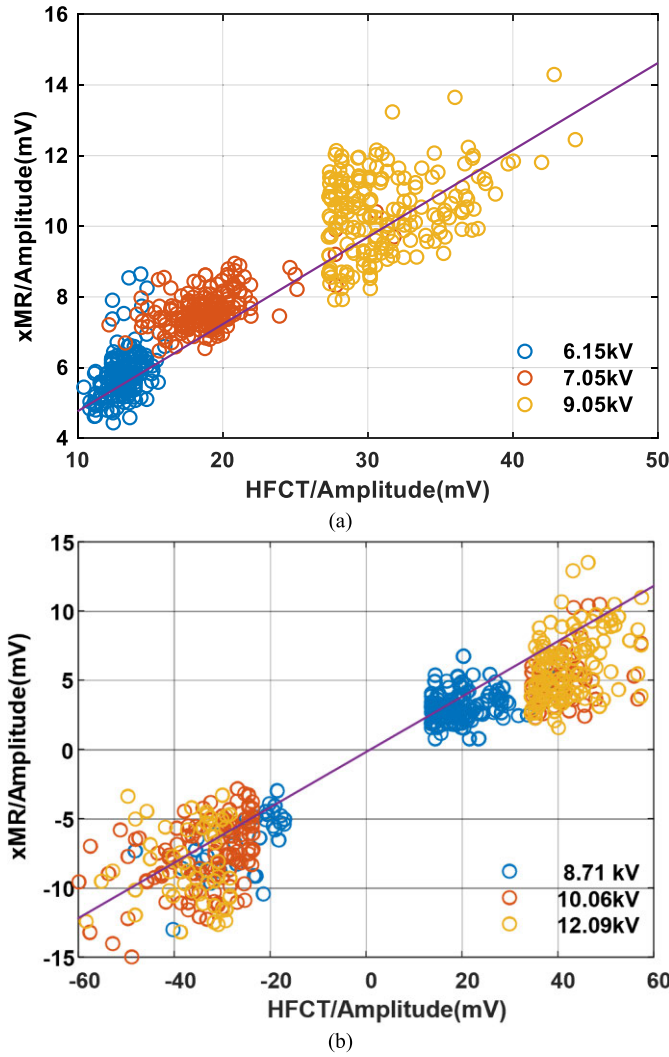


Fig. 18. Correlation between HFCT and xMR signals. (a) Corona. (b) Surface.

Since the xMR sensor is located close to HV potentials, the correctness in the polarity proves that the xMR system is predominantly reacting to the magnetic field of the PD while rejecting its electric field.

In general, there is a clear proportional correlation between the peak value of the HFCT and xMR signals amplitude.

Note that at higher voltages, the data become scattered. The waveforms corresponding to each data point in Fig. 18 are checked. In some cases, it is found that the xMR signals are distorted by low-frequency noise in the pre-trigger data of the signals as well as by oversampling that adds high-frequency noise. To calculate the peak amplitudes, the PDflex software tool attempts to detect and remove the offset of each signal. However, the result of this routine not always yields optimal results for all the data sets, which leads to errors in the peak amplitudes and, therefore, to an increase in the scatter in Fig. 18. Another reason for the scatter is that the HFCT measures the PD conduction currents while the xMR system measures the near-field magnetic fields of the PD events. PD current pulses may happen in different directions. The xMR system is unidirectionally sensitive, which does not apply to the HFCT. This affects the correlation between the

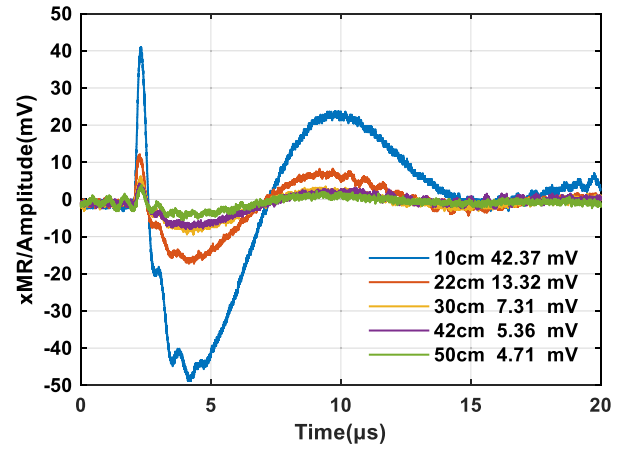


Fig. 19. xMR signals variation with distances.

two measuring methods. The combination of these effects is regarded to yield the clouds in Fig. 18.

Next, concerning position 2 of the xMR system [Fig. 10(b)], the largest negative corona pulses from the xMR system under different distances from 10 to 50 cm are chosen as a case study, as shown in Fig. 19. The xMR system output voltage has an inverse correlation with the distance. Consequently, it can be confirmed that the xMR system mainly captures the magnetic field emitted by PD currents with frequencies located within its bandwidth.

The Biot-Savart Law describes the magnetic field generated by an electric current flowing through a conducting wire, as in the following formula:

$$B = \frac{\mu_0 I}{4\pi d} (\cos \theta_1 - \cos \theta_2) \quad (3)$$

where B is the magnetic flux density, μ_0 is the vacuum permeability, I is the electric current flowing through the conducting wire (PD loop), d is the vertical distance between the sensor and the corona, and θ_1 and θ_2 are the function of d , which represent the angles between the wire and the vectors from the sensor to both ends of the wire.

The average amplitudes of the xMR signals at several distances are shown in Fig. 20. Substituting the actual data into formula (3), the theoretical values of B with increasing distance d are also calculated. Then, the Method of Least Squares is used to find the optimum fit of theoretical values for the measured xMR amplitudes of $y(d)$, as in the following formula [22]:

$$y(d) = a \cdot f(d) + b \quad (4)$$

where $f(d)$ is the Biot-Savart Law for d . The Least Squares fitting of Biot-Savart Law is shown in Fig. 20, in which $a = 0.163 \text{ mV/pT}$, and $b = 2.85 \text{ mV}$.

Clearly, the changing trend of the experimental results is consistent with the theoretical values, indicating an approximately inverse relationship between the xMR signals and the distance from the xMR sensor to the corona. At 50 cm, the xMR signals have an average amplitude of 3.2 mV.

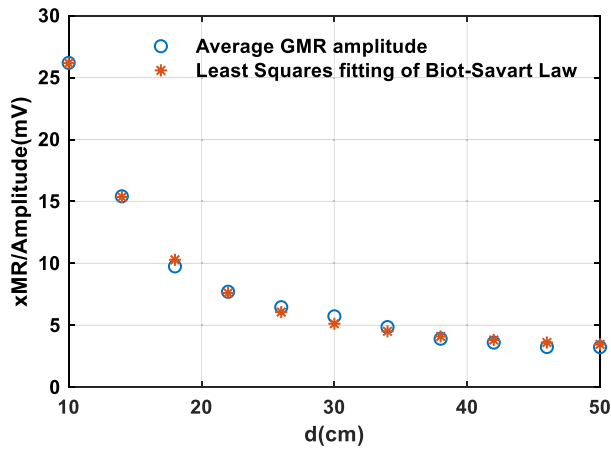


Fig. 20. Relationship between the xMR signals and the distance from the xMR sensor to the corona.

D. XLPE Cable With the Artificial Defect

The results in Section IV-C show that the xMR system is sensitive to PD events even when the sensor is located tens of cm away from the PD source. This then opens the possibilities for its application in detecting PD activity in HV cables. With this purpose, another PD experiment has been performed on the XLPE cable with an artificial defect. The PRPD patterns obtained from the HFCT and the xMR system are depicted in Fig. 21, using the xMR signals as the trigger sources.

The comparison between the PD detection using the HFCT and the xMR system shows no major differences in the PRPD patterns.

Due to the spatial sensitivity of the xMR sensor, several attempts to change its orientation are needed before the output of the xMR system is enough to trigger the oscilloscope. As seen in Fig. 12, it turned out that the best position of the xMR sensor is parallel to the cable joint. It is also worth noting that the sensor is placed close but not exactly on top of the PD defect. For these experiments, its orientation plays a more dominant role than its location relative to the PD defect.

E. Discussions

This article clearly confirms that the xMR sensor is sensitive to measuring the magnetic field produced by the PDs. The sensor can be placed externally to suspect spots in the insulation or ground wires while remaining contactless.

At this phase of the development of the xMR system, limitations such as the systems' bandwidth remain to be addressed. As has been mentioned, the xMR sensor's associated circuitry limits its bandwidth. Further developments related to electronic techniques are needed to overcome this limitation.

Even in its current development state, the xMR system's sensitivity is remarkably high. The detection of the PD events from the corona and surface models proves useful to verify the correct functioning and performance of the xMR system, but its sensitivity with increasing distance boosts the potential of the xMR system to be used as a contactless method in actual HV cables. Moreover, the results in Fig. 21 prove not

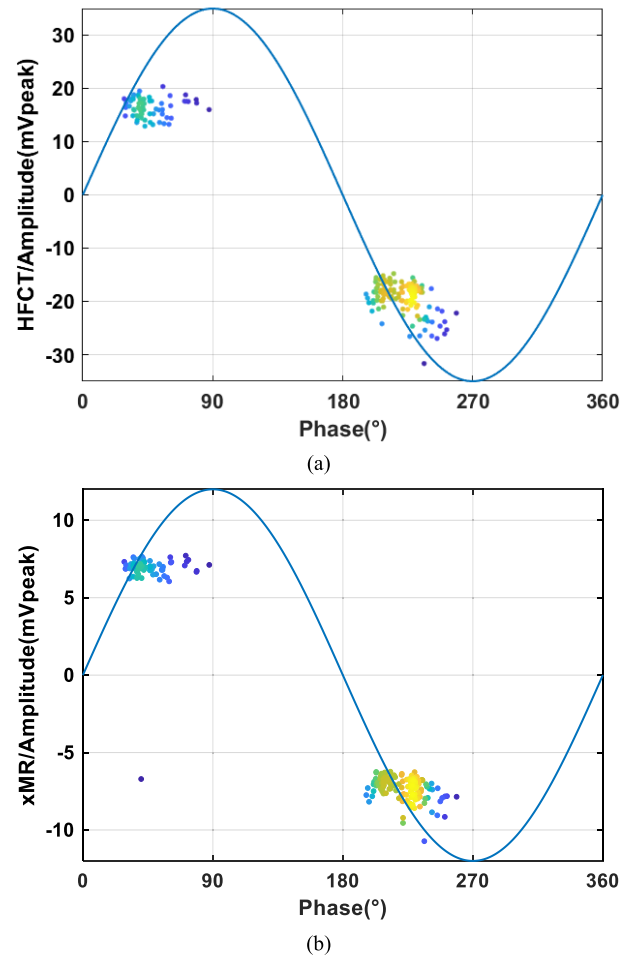


Fig. 21. PRPD patterns of the cable with the artificial defect using the xMR signals as trigger sources. (a) HFCT. (b) xMR system.

only that the xMR system is sensitive to part of the magnetic field that leaks out of the HV cable through the ground sheath but that the sensor position is not restrained to the vicinity of the PD defect. The PD signals travel along the cable as in a transmission line, implying that the xMR sensor can be placed away from the PD source.

In a second series of this research, we report an extended set of measurement results from the HV cable. The tests included an improved system bandwidth, the nominal current flowing in the HV cable, and the position of the sensor 1 m away from the PD source.

V. CONCLUSION

In this article, an alternative approach to detect PD signals without contact based on magnetic field detection using an xMR sensor is proposed. An improved design of the signal conditioning circuit for the xMR sensor has been reported. The following conclusions are drawn.

The xMR sensor with the implemented circuit has a broad bandwidth up to the range of MHz. Further extension of the circuit's bandwidth is under investigation.

The xMR system can detect PD pulses with a minimum amount of 50 pC from a PD pulse calibrator, which preliminarily verifies its possibility to detect PDs.

Experimental results for the corona and surface PD models provide close results compared to an HFCT concerning the PD pulses and PRPD patterns.

The absolute value of the HFCT and xMR signals are proportional, which illustrates that the xMR system can effectively respond to the PD magnitude and reflect the PD intensity well. However, for time-resolved PD analysis, more bandwidth is still needed.

The results have shown that the xMR system is sensitive to detecting small discharges, for example, with an average output amplitude of 3.2 mV at 50 cm from the corona. An inverse relationship exists between the xMR system output voltage and the distance from the corona, which is in accordance with the Biot-Savart Law.

The methodology presented in this article has led to successful measurements in laboratory PD experiments using corona and surface PD models. Practical verification based on a 6/10 kV XLPE cable also shows the ability of this xMR system for non-contacting PD detection. In the next stage, the performance of this xMR system has to be checked with different discharge defects for PD sources identification, location, and in different types of power equipment like power cables and gas-insulated systems (GIS), which is also the main research contents of our second publication.

ACKNOWLEDGMENT

The authors are grateful to Geert Jan Kamphuis, Wim Termorshuizen, and Paul van Nes from the High Voltage Laboratory of the Delft University of Technology for their experimental support in using the HV facilities.

Yun Chen also gratefully acknowledges her supervisors, Academician Licheng Li and Prof. Yanpeng Hao at the South China University of Technology, and Prof. Mingli Fu at Electric Power Research Institute of China Southern Grid, for their support, encouragement, and guidance.

The authors would like to thank TDK Corporation for supplying the Nivio xMR sensors for this research.

REFERENCES

- [1] J. Li, H. Liu, and T. Bi, "Tunnel magnetoresistance-based noncontact current sensing and measurement method," *IEEE Trans. Instrum. Meas.*, vol. 71, pp. 1–9, 2022.
- [2] Z. Li et al., "A pulse interference suppression method based on double-sensor detection for PD measurement in frequency-tuned resonant tests," *IEEE Trans. Instrum. Meas.*, vol. 71, pp. 1–8, 2022.
- [3] Y. Zang, Y. Qian, X. Zhou, A. Xu, G. Sheng, and X. Jiang, "Application of a partial discharge diagnosis method based on the novel multispectral array sensor and GMM in different insulating gases," *IEEE Trans. Instrum. Meas.*, vol. 71, pp. 1–11, 2022.
- [4] Y. Chen et al., "Voltage equivalence of partial discharge tests for XLPE insulation defects," *IEEE Trans. Dielectr. Electr. Insul.*, vol. 29, no. 2, pp. 683–692, Apr. 2022.
- [5] Y. Ouyang et al., "Current sensors based on GMR effect for smart grid applications," *Sens. Actuators A, Phys.*, vol. 294, pp. 8–16, Aug. 2019.
- [6] R. Weiss, R. Mattheis, and G. Reiss, "Advanced giant magnetoresistance technology for measurement applications," *Meas. Sci. Technol.*, vol. 24, pp. 1–17, Jul. 2013.
- [7] C. Reig, M.-D. Cubells-Beltrán, and D. R. Muñoz, "Magnetic field sensors based on giant magnetoresistance (GMR) technology: Applications in electrical current sensing," *Sensors*, vol. 9, no. 10, pp. 7919–7942, Oct. 2009.

- [8] S. Yang and J. Zhang, "Current progress of magnetoresistance sensors," *Chemosensors*, vol. 9, no. 8, pp. 1–23, Aug. 2021.
- [9] P. P. Freitas, R. Ferreira, S. Cardoso, and F. Cardoso, "Magnetoresistive sensors," *J. Phys., Condens. Matter*, vol. 19, no. 16, 2007, Art. no. 165221.
- [10] M. Díaz-Michelena, "Small magnetic sensors for space applications," *Sensors*, vol. 9, no. 4, pp. 2271–2288, Mar. 2009.
- [11] J. Lenz and A. S. Edelstein, "Magnetic sensors and their applications," *IEEE Sensors J.*, vol. 6, no. 3, pp. 631–649, Jun. 2006.
- [12] M. A. Khan et al., "Magnetic sensors-a review and recent technologies," *Eng. Res. Exp.*, vol. 3, no. 2, pp. 1–22, Jun. 2021.
- [13] Y. Ouyang, J. He, J. Hu, and S. Wang, "A current sensor based on the giant magnetoresistance effect: Design and potential smart grid applications," *Sensors*, vol. 12, no. 11, pp. 15520–15541, Nov. 2012.
- [14] G. Zhao, J. Hu, Y. Ouyang, Z. Wang, S. X. Wang, and J. He, "Tunneling magnetoresistive sensors for high-frequency corona discharge location," *IEEE Trans. Magn.*, vol. 52, no. 7, pp. 1–4, Jul. 2016.
- [15] C. Muşuroi et al., "High sensitivity differential giant magnetoresistance (GMR) based sensor for non-contacting DC/AC current measurement," *Sens.*, vol. 20, no. 323, pp. 1–17, Jan. 2020.
- [16] Y. Li and Z. Qian, "The application of GMR sensor in the partial discharge detection," in *Proc. Int. Conf. Condition Monitor. Diagnosis (CMD)*, Sep. 2016, pp. 924–927.
- [17] S. B. Trisnanto et al., "Magnetic particle imaging using linear magnetization response-driven harmonic signal of magnetoresistive sensor," *Appl. Phys. Exp.*, vol. 14, Aug. 2021, Art. no. 095001.
- [18] Z. Li and S. Dixon, "A closed-loop operation to improve GMR sensor accuracy," *IEEE Sensors J.*, vol. 16, no. 15, pp. 6003–6007, Aug. 2016.
- [19] E. Hirota, H. Sakakima, and K. Inomata, *Giant Magneto-Resistance Devices*. Cham, Switzerland: Springer, 2002.
- [20] A. R. Mor, L. C. C. Heredia, D. A. Harmsen, and F. A. Muñoz, "A new design of a test platform for testing multiple partial discharge sources," *Int. J. Electr. Power Energy Syst.*, vol. 94, pp. 374–384, Jan. 2018.
- [21] PDFflex. *Unconventional Partial Discharge Analysis*. Accessed: Apr. 28, 2023. [Online]. Available: <http://pdflex.tudelft.nl>
- [22] S. J. Miller, "The method of least squares," *Math. Dept. Brown Univ.*, to be published.



Yun Chen was born in Guangdong, China, in 1993. She received the B.S. degree from the South China Agricultural University, Guangzhou, China, in 2016, and the M.S. degree from the South China University of Technology, Guangzhou, in 2019, where she is currently pursuing the Ph.D. degree.

She is an Academic Guest at the High Voltage Technologies Group, Delft University of Technology, Delft, The Netherlands. Her research interests include high-voltage technology and partial discharge testing of electric power equipment.



Luis Carlos Castro Heredia was born in Cali, Colombia, in 1986. He received the B.S. and Ph.D. degrees from the Universidad del Valle, Cali, in 2009 and 2015, respectively.

He worked as a Researcher at the High Voltage Technologies Group, Delft University of Technology, Delft, The Netherlands, from 2016 to 2022. He will become a Senior Analog Electronics Designer at Sioux Technologies, Eindhoven, The Netherlands, in 2023. His research interests include high-voltage technology, partial discharge

testing, analog electronics, and sensor interfacing.



Johan J. Smit (Member, IEEE) was born in Dordrecht, The Netherlands, in 1949. He received the M.S. degree from the University of Amsterdam, Amsterdam, The Netherlands, in 1974, and the Ph.D. degree from the State University of Leiden, Leiden, The Netherlands, in 1979.

He became a full Professor at the Delft University of Technology, Delft, The Netherlands, in 1995, and has served as emeritus since 2015. Earlier, he was employed at the Kamerlingh Onnes Laboratory, Leiden, at KEMA's Engineering Company from 1979 to 1999, on the supervisory board of the South Holland Power Grid from 1999 to 2004, as a General Chairperson of the International Symposium on HV Engineering in 2003, and a CEO at the foundation KSANDR in the field of T&D Asset Management from 2003 to 2015. In CIGRE, the global International Council on Large Electric Systems, he chaired the International Study Committee D1 on Materials and Emerging Technologies from 1992 to 2004, and he convened the area Substation Management for SC B3 since 2005. His standardization activities include the national chairmanship of the board of the Royal Dutch Electrotechnical Committee (NEC-NL) since 2020, and the international chairmanship of IEC TC 112, Electrical Insulation Materials and Systems, since 2018. His research focuses on super/smart/sustainable high voltage solutions for power grids.



Robert Ross (Senior Member, IEEE) was born in Rotterdam, The Netherlands, in 1958. He received the M.S. and Ph.D. degrees from the Utrecht University, Utrecht, The Netherlands, in 1986 and 1990, respectively.

He is a Professor at the Delft University of Technology, Delft, The Netherlands, a Director of IWO (Institute for Science and Development), a Professor at the HAN University, Arnhem, The Netherlands, and an Asset Management Research Strategist at TenneT (TSO in The Netherlands and part of Germany). At KEMA, he worked on reliability and post-failure forensic investigations. He recently wrote the Wiley/IEEE book "Reliability Analysis for Asset Management of Electric Power Grids" based on his experience with utilities and the navy. His special fields of interest are reliable and sustainable energy supply and innovations like superconductivity and power electronics for the next generation grids.

Dr. Ross was a recipient of SenterNovem Annual Award and nominated for Best Researcher by the World Technology Network for energy inventions. He was active in various committees in CIGRE, IEC, IEEE, and IEE.



Mohamad Ghaffarian Niasar was born in Tehran, Iran, in 1984. He received the M.S. degree from the Sharif University of Technology, Tehran, in 2008, and the Ph.D. degree from the Royal Institute of Technology, Stockholm, Sweden, in 2015.

He is currently an Assistant Professor at the High Voltage Technologies Group, Delft University of Technology, Delft, The Netherlands. His main research interests are the aging of electrical insulation, HVDC insulation system, partial discharges, high-frequency power transformers, power cables, and FEM modeling.